Journal Title
XX(X):2–20
©The Author(s) 2016
Reprints and permission:
sagepub.co.uk/journalsPermissions.nav
DOI: 10.1177/ToBeAssigned
www.sagepub.com/
SAGE

# Extremely Deformable Morphing Leading Edge: Optimization, Design and Structural Testing

**Anton Rudenko[1], André Hannig[2], Hans Peter Monner[1] and Peter Horst[2]**

**Abstract**

The future generation of high-lift devices need to be improved to reduce the noise footprint and increase the performance for take off and landing of transport aircraft. To contribute to these goals, an active blown Coandă flap-based high-lift system is being investigated within the German national Collaborative Research Centre 880 as an alternative to the state of the art flaps. A key part of this system is an adaptive gapless droop nose with extremely large morphing deformation. The design and construction of this component is based on a structural optimization framework. The framework consists of two hierarchical design steps, an optimization of the hybrid composite skin layout with integral T-stringers, acting as joints to the inner actuation mechanism and the kinematic optimization of the latter. A hybrid skin structure allows a large curvature to rupture in the morphing direction, while providing high stiffness in the transverse direction. This paper describes a full-scale hybrid composite morphing droop nose and its structural tests. The results of these tests are finally compared to the finite element simulation and applied for validation of the optimization framework. A sensitivity analysis is provided to evaluate the influence of modelling and manufacturing uncertainties to the shape quality.

**Keywords**

leading edge, morphing, adaptive structures, full-scale, structural demonstrator, hybrid, composites

*Prepared using* sagej.cls *[Version: 2015/06/09 v1.01]*

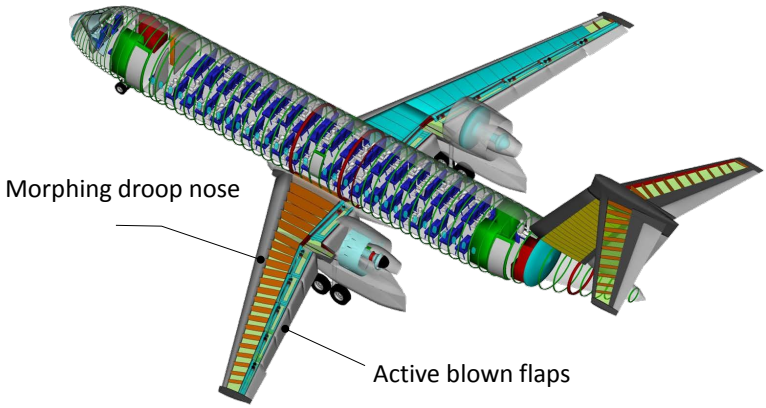


**Figure 1.** The CRC 880 application scenario: regional aircraft with short take off and landing capabilities

## Introduction

The vision 2050 of the ACARE group in the ACARE 2050 (2011) provides the goals for the reduction of emissions in commercial aircraft of the future. The proposed aim is to achieve 75% CO2, 90% NOx and 65% perceived noise reduction until 2050, relative to the capabilities of typical new aircraft in 2000. An additional goal is to provide the possibility to complete their journey, door-to-door within 4 hours to 90% of travelers within Europe. Similar aims are provided by the Federal Aviation Administration in FAA (2015) for the US market. To handle these aims, a novel concept of a high efficient and low noise regional aircraft is being investigated within the German national Collaborative Research Center (SFB) 880. In order to achieve such substantial reductions it is necessary to work on all contributing aircraft systems such as the engines, landing gear and the wings themselves. A conceptual application scenario, presented in Figure 1, is designed within the CRC 880 framework for technological and economical assessment of investigated technologies. A detailed description of the evaluation and design process is presented by Heinze and Radespiel (2014).

[1]Institute of Composite Structures and Adaptive Systems, German Aerospace Center, Braunschweig, Germany
[2]Institute of Aircraft Design and Lightweight Structures, TU Braunschweig, Germany

**Corresponding author:**
Anton Rudenko, Institute of Composite Structures and Adaptive Systems, Lilienthalplatz 7, 38108 Braunschweig, Germany
Email: anton.rudenko@dlr.de

*Prepared using* sagej.cls

In particular the high-lift system is identified by Kreth and Wild (2007) as a dominant source of airframe noise during the approach and landing procedures. One possibility to reduce this noise is to apply an active blown high-lift system as presented in Figure 2. The concept benefits from the Coandă effect and enables very high lift coefficients. Consequently, steeper descent and approach operations along with shorter runway lengths would be possible for novel regional aircraft.

Recent investigations such as Burnazzi and Radespiel (2014) have demonstrated that such a high-lift solution benefits significantly from a gapless and stepless adaptive leading edge device. A number of concepts for adaptive aircraft structures were presented during the last decade with a wide range of structural and application scenarios: beginning with wing tip and camber morphing (Radestock et al. (2015), Takahashi et al. (2016), Falcao et al. (2011)) up to folding or telescopic extension of the whole wing (Ajaj and Friswell et.al (2016), Gamboa and Santos (2016)). A broader overview can be found in Barbarino et al. (2011), Weisshaar (2013) and Sun et al. (2016). Regarding the previously mentioned adaptive droop nose technology, different concepts were presented as well: on the one hand some topology optimization approaches by Lu and Kota (2005) and De Gaspari and Ricci (2011) with a Load Path Generation method and by Vasista et al. (2016) with the Solid Isotropic Material with Penalization (SIMP) method, but also joints and struts based systems, e.g. by Kintscher et al. (2015), on the other.

These investigations cover a wide range of activities: numerical simulations (finite element (FE) method and computational fluid dynamics (CFD)), experiments using prototype models, wind tunnel demonstrations and flight tests with morphing wings. Thereby it is demonstrated, that the development of morphing aircraft structures results from overall considerations of aerodynamics, structures, control dynamics and manufacturing. Therefore, drive demonstration and structural evaluation through a full-size model are essential parts for the feasibility validation of a morphing leading edge.

In this paper, the key characteristics of a curvature morphing skin structure are presented. These skin parameters in turn serve as input for the following optimization. First structural optimization process of the whole droop nose is then outlined from the tailoring of the skin up to the validation of the process via experimental testing of a manufactured fully functional full-scale droop nose segment. Experimental results are evaluated and discussed within a sensitivity consideration of modelling and manufacturing parameters to the shape and curvature of the morphing leading edge.

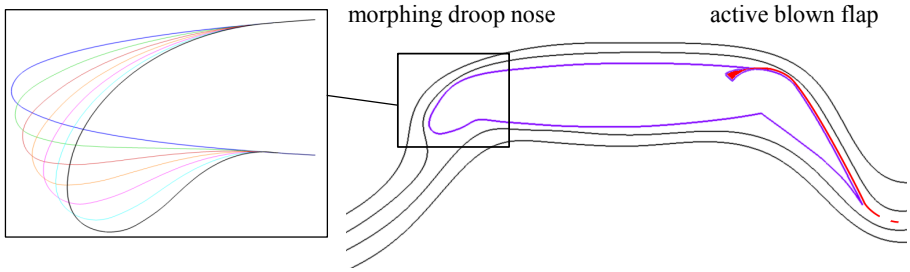


**Figure 2.** Coandă-flap (right) based high-lift system and the deflection of the adaptive droop nose (left).

## Morphing skin design

The aim of this section is to present relevant aspects of the droop nose skin, which are needed for the subsequent optimization process.

The main characteristics of the curvature morphing skin is a high curvature at rupture and thus bending normal strain in morphing direction. Simultaneously, the spanwise stiffness has to be maximized in order to sustain aerodynamic loads and thus to reduce the number of required kinematic ribs. Similarly to other morphing concepts, these contradictory requirements are fulfilled by imposing an extreme anisotropy of the skin structure. An outstanding issue of curvature morphing skins is the need of a frequent change in bending stiffness along it's perimeter (strongly depends on the actuation type). Additionally, this skin is intended to be applied in a full-scale demonstrator. For these reasons, a layered structure is chosen which enables almost standard composite tooling.

The concept of the skin is given in Figure 3. It consists of a centred GFRP laminate and additional outer hybrid layers. Herein, the inner layers are primarily responsible for the stiffness tailoring in morphing direction (s-direction) and also the critical component regarding maximum achivable curvature or bending strain, respectively. In contrast, the hybrid layers add significant span-wise bending stiffness (y-direction), cp. Figure 6.

The hybrid layers consist of discrete composite bundles which are embedded in an elastomeric foundation. Thus, bending normal strain is taken by the elastomer while the discrete stiffeners remain intact. Note that compounding fibres directly into an elastomer (known as chord-rubber composites) results in very poor performance in case of compression in fibre direction (thus also for bending). The buckling behaviour of these discrete rods within the elastomeric foundation was recently investigated, see Schmitz and Horst (2015-2).

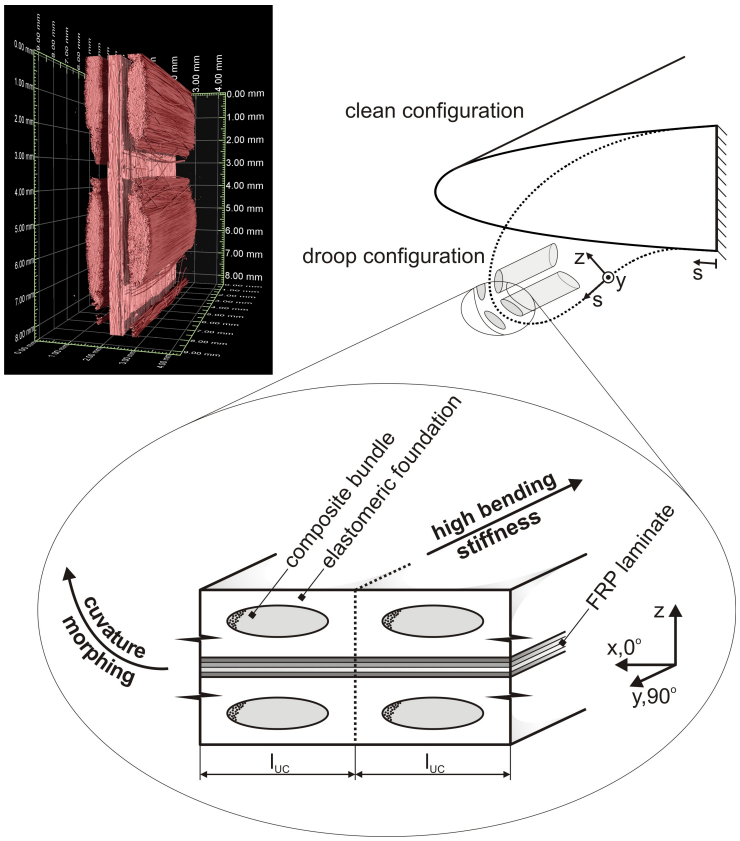


**Figure 3.** Sketch of the structural concept of the leading edge skin. The microtomography scan shows the structure without the elastomeric foundation.

During the investigation of the hybrid structure, two different materials and corresponding manufacturing processes were established. Firstly, a sufficient transparent thermoplastic polyurethane (TPU) elastomer was combined with glass-fibre/epoxy bundles in order to enable visible detection of damages during mechanical testing. It can be stated, that the only observed damage mode is transverse cracking inside the bundles (interface damages between stiffener and foundation do not occur). Additionally, transverse cracking onset could be well predicted via a FE unit-cell, see Schmitz and Horst (2014). Secondly, EPDM rubber was combined with unidirectional HeyPly® 913 prepreg, as this combination offers better manufacturability, see Schmitz and Horst (2015) for details. Therefore, this material combination is used for the demonstrator. It can be stated, that concepts and first tests regarding abrasion, lightning-strike and anti-icing problems are available.

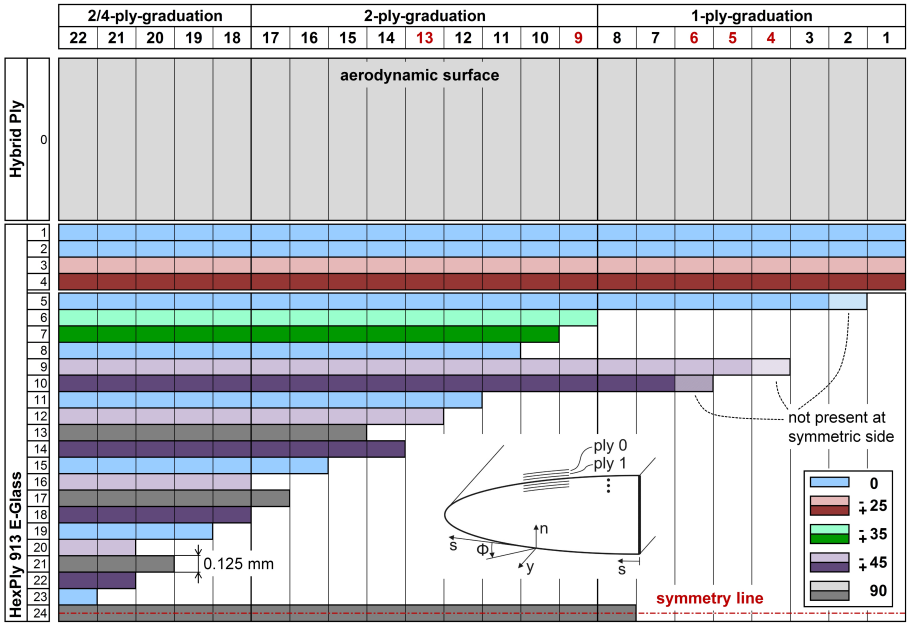


**Figure 4.** Layups of predefined skin segments.

## *Skin segments*

As stated, the inner layers of the skin structure are responsible for the bending stiffness tailoring along the skin perimeter. Due to the key requirement of a large strain to failure in morphing direction, a glass-fibre composite stacked up from $0.125\ \mathrm{mm}$ UD E-glass HexPly® 913 is used. Composite constructions inherently show step-wise thickness alterations as these are realized via ply counts. This means that the bending stiffness of the skin can not be optimized by simply local continuously changing thickness. Hence, 22 discrete skin segments are predefined, cp. Figure 4. Serving as input, these are placed by the following optimization.

At this point, a 2D segment of the droop nose, cp. Figure 11, is developed. Thus, constant span-wise stiffness is added in terms of two constant hybrid layers, see Figure 4. The thickness of such hybrid layer denotes $1.28\ \mathrm{mm}$. Detailed geometrical and mechanical properties data can be found in Schmitz and Horst (2015-2), as exactly the same structure is investigated there. However, in order to easily deal with the hybrid layers in terms of the classical laminated plate theory (CLP), engineering properties are extracted. This is done by a representative FE unit-cell (RVE), which is able to calculate a whole CLP stiffness matrix including all bending and coupling terms for a modelled structure, see Schmitz and Horst (2014-2). As the centred laminate serves as boundary

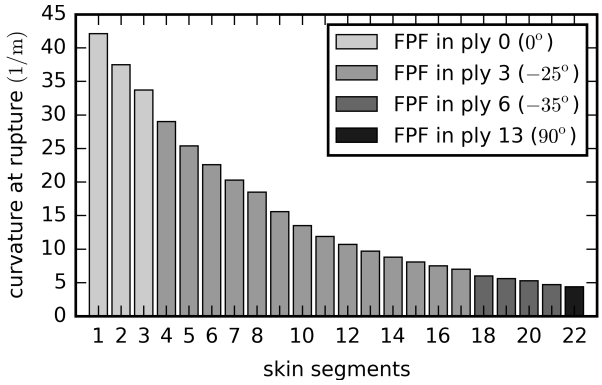


**Figure 5.** Curvature at rupture of predefined skin segments. The location of first ply failure (FPF) calculated via the Puck failure criterion is indicated.

condition for the hybrid layers, a homogenized CLP stiffness matrix is calculated for the stacking $[90_{\text{hybrid}}, 0_8, 90_{\text{hybrid}}]$. As bending properties are most relevant for the droop nose, engineering properties for a single hybrid layer are recalculated from the $\mathbf{D}$ matrix (bending representation) of the CLP stiffness matrix: $E_y = 8454$ MPa, $E_s = 29$ MPa, $G_{sy} = 20$ MPa and anticlastic bending ratio (bending equivalent to in-plane poisson's ratio) $\nu^{\text{b}}_{sy} = 0.001$.

Due to the strongly dominant bending strain, the design loadcase for the 2D droop nose segments in terms of failure are chosen to

$$(\epsilon_s, \epsilon_y, \gamma_{sy}, \kappa_s, \kappa_y, \kappa_{sy})^T = (0, 0, 0, \kappa_{crit}, 0, 0)^T \tag{1}$$

meaning a deformation determined curvature in morphing direction with retarded anticlastic bending deformations. The critical strain $\kappa_{crit}$ is determined via the well known Puck criterion. The critical bending strain for each segment used for the optimization later on is then calculated via

$$\epsilon_{crit} = \frac{1}{2}\,\kappa_{crit}\,t_{GFRP}\,. \tag{2}$$

Herein, $t_{GFRP}$ is the total thickness of the centred laminate only, as the used hybrid layers show much larger curvatures at rupture. These are calculated with the mentioned RVE and 3D Puck criterion. This method is validated with experiments in Schmitz and Horst (2014). For the presented hybrid layer at skin segment 1 it gives a critical curvature of 268 $1/\text{m}$. The critical curvatures of all segments are given in Figure 5. The corresponding bending stiffness in morphing $EI_{s,total}$ and span-wise directions

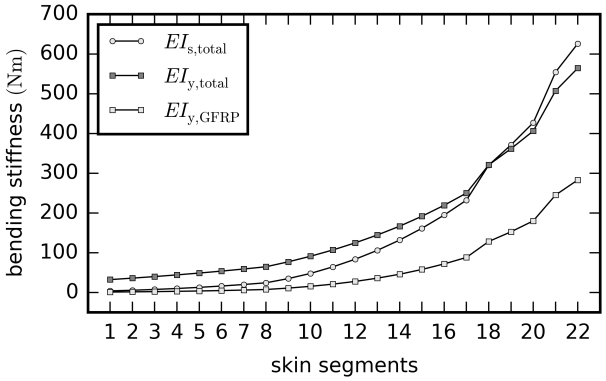


**Figure 6.** Bending stiffness of skin segments.

$EI_{y,total}$ are presented in Figure 6. Herein, $EI$ is defined as bending stiffness per width, namely $EI = 1/12\, E\, t_{total}^3$ with $E$ as homogenized modulus extracted from the $\mathbf{D}$ matrix. Figure 6 clearly indicates the benefit of the hybrid layers: the bending stiffness with hybrid layers $EI_{y,total}$ is much higher than with centred GFRP laminate only, $EI_{y,GFRP}$. Especially in the first segments there is a factor of approximately 30 between these two. Additionally, the anticlastic bending behaviour of the skin is strongly reduced due to the large bending stiffness in span-wise direction. In case of the first segment the anticlastic ratio without hybrid layers reads $\nu_{sy}^{\mathrm{b,GFRP}} = 0.345$ compared to $\nu_{sy}^{\mathrm{b,total}} = 0.013$ with hybrid layers. This is especially advantageous at free edges in order to maintain the curvature at rupture and the aerodynamic profile.

Finally, the main reasons for choosing the layup shown in Figure 4 are outlined:

(i) relative bending stiffness steps from one segment to its particular neighbours due to ending plies should not exceed a maximum of $1.50$ in order to maintain a smooth curvature in morphing direction. This is the reason for the 1-ply, 2-ply and 2/4-ply-graduation parts (Figure 4). Hence, a minimum number of different segments is achieved. Actually, the largest steps occur from segment 8 to 9 (difference of $1.43$) and from 1 to 2 (difference of $1.40$).

(ii) occurrences of $0^{\mathrm{o}}/90^{\mathrm{o}}$ plies and identical angles of adjacent plies are kept to a minimum.

(iii) ending plies are always placed near the elastic bending axis in order to locate such potential initiator of premature failure in lower stress regions.

(iv) the curvature at rupture in morphing direction is maximized. Nevertheless, as much as possible shear stiffness is added especially in the first segments. This

is important in view of the coming 3D droop nose investigations, because span-wise wing deflections will generate considerable shear fluxes in the closed profile of the nose, which is rigidly connected to the wing box.

(v) the span-wise bending stiffness is maximized via the constant hybrid layers. This will reduce the number of needed kinematic ribs in span-wise direction.

(vi) all layups are symmetric resulting in zero in-plane/out-of-plane couplings ($\mathbf{B} = \mathbf{0}$). Where possible the layups are also balanced, which gives a minimum coupling within the $\mathbf{A}$ und $\mathbf{D}$ CLP matrices. In case of the marked segments in Figure 4 (4, 5, 6, 9, 13) the latter aspect is violated in favour to previous considerations (angle-plies are already added (iv) but only a 1 step gradation is possible due to (i)).

(vii) a small skin thickness is a general problem of such leading edge device regarding impact issues. Thus, the hybrid layers are advantageous, too. Segment 1 has the minimum occurring total thickness of $3.57\ \mathrm{mm}$.

(viii) due to manufacturability, the minimum length along the nose's perimeter of a segment is set to $10\ \mathrm{mm}$.

(ix) within the optimization, all segments must be used when tailoring from a thin to a thick segment. This avoids thick ply discounts and ensures a smooth curvature.

## Optimization framework

The idea of the presented morphing droop nose is based on the research of Kintscher and Heinze (2010). The supplementary challenge in this work however, is the exceedingly high (approx. 300% more than achieved before) amount of the leading edge morphing, which is aerodynamically required by the active-blown flap. This results in a innovative skin structure, inward mechanism and novel force transmission interfaces between these two parts. The concept of the skin optimization is based on stiffness modification of the leading edge skin along its perimeter in chord direction, considering the target deformation and maximum strain. Furthermore, a reliable application of the actuator forces to a thin-walled, highly deformed hybrid composite skin structure has to be ensured.

The initial conditions for the optimization are formed by the target shapes of the airfoil for cruise and high-lift conditions. These shapes are stated by aerodynamic quality on the one hand and by the requirement of a constant skin length on the other. The letter restriction prevents non-bending strains in the skin and thus reduces the strain level. A detailed description of a shape generation is presented by Burnazzi and Radespiel (2014).

Based on the above definitions, the optimization is structured as shown in the process diagram in Figure 7. The first step is a creation of a finite element model of the morphing leading edge. Then, nonlinear calculations have to be performed for both relevant load cases (cruise and high-lift) with associated aerodynamic loads and kinematic displacements. In the first load case, the kinematic system is assumed to be rigid and to act like a normal rib. In the second case, the force application points are displaced accordant to the parameter definitions of the inward mechanism. The results of the calculation (strains and local/global displacements) are stored for further evaluation.

### *Optimization parameters*

In conventional structure design, the skin thickness has to be increased in critical regions to prevent the leading edge structure from undesirable deformations. In case of morphing structures, such approach results in high strains in the outer skin layers. Due to such contradictory requirements, the skin stiffness tailoring has to be a part of an optimization process.

That process is based on the stiffness adjustment along the skin perimeter, bearing in mind the target deformation for high and low speed load cases, maximum strain as well as internal and external loads. The presented droop nose concept allows to adjust the following set of parameters (shown in Figure 8):

(i) predefined stacking segment, see Figure 4. Thus, the possibility of adjusting the number of plies with corresponding ply angles in each skin segment along the perimeter
(ii) positions of the force application interfaces (stringers)
(iii) direction and magnitude of the kinematic forces at the interfaces

### *Objective function*

The objective function is based on a weighted addition of the relevant criteria, which are summarized in Table 1. The criteria are normalized and have to be evaluated with appropriate weighting factors according to following equation:

$$\Phi = \alpha \sum \sqrt{\left(\kappa_{d,t} - \kappa_{d,i}\right)^2} + \theta \cdot max\Delta_{s,d} + \beta \cdot max\Delta_{s,c} + \gamma \left[\epsilon_{max} - \epsilon_{crit}\right] \quad (3)$$

The terms of the objective function are grouped in three sections , namely

(i) curvature

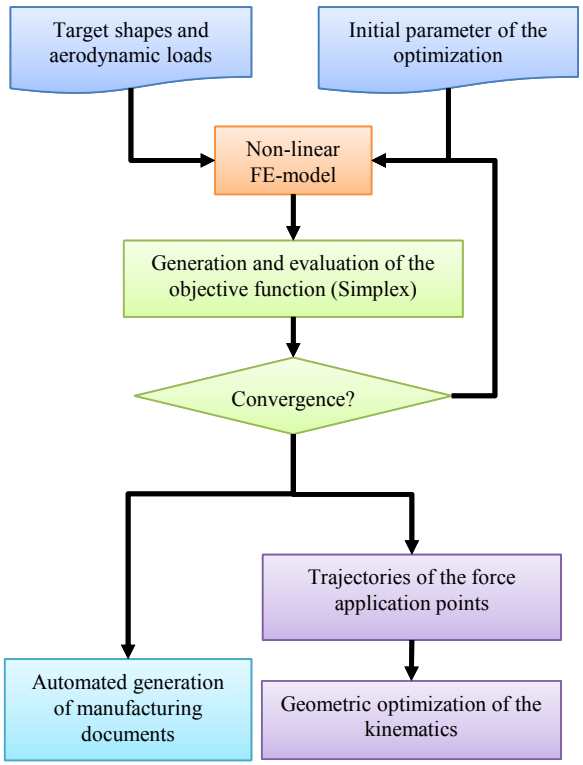


**Figure 7.** Optimization strategy for the morphing droop nose.

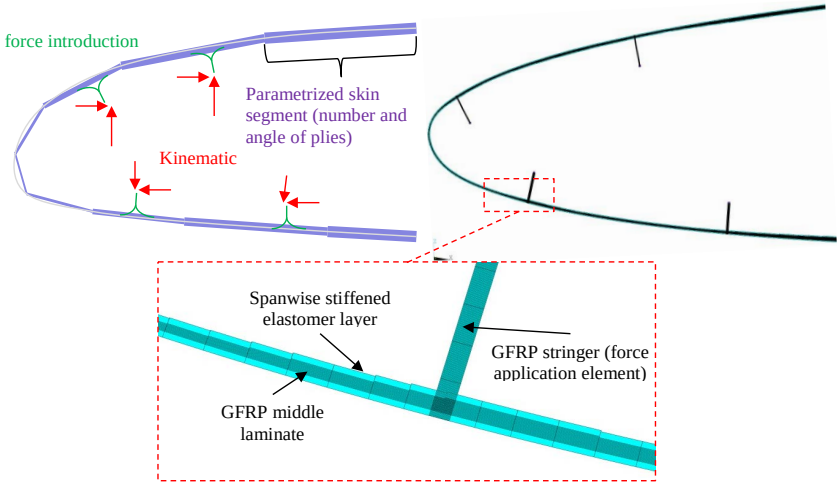


**Figure 8.** Parametrization and modelling of the morphing skin.

**Table 1.** Components of the additive objective function

| Parameter | Description |
|---|---|
| $\kappa_{d,t}$ | target curvature of the outer skin surface |
| $\kappa_{d,i}$ | calculated curvature of the outer skin surface |
| $max\Delta_{s,d}$ | maximum deviation from the target skin shape in high-lift conditions |
| $max\Delta_{s,c}$ | maximum deviation from the target skin shape in cruise conditions |
| $\epsilon_{max}$ | maximum strain in the outer GFRP layer |
| $\epsilon_{crit}$ | maximum allowable strain |
| $\alpha,\ \beta,\ \gamma,\ \theta$ | weighting factors for the additive objective function |

(ii) shape

(iii) maximum structural strain in the outer layer

This kind of definition allows the control of the optimization regarding the desired result: for example, the curvature influence can be increased for aerodynamically driven application like the presented droop nose. According to this, the numerical values of the weighting factors have to be determined empirically in order to enhance the convergence behaviour of the process or to define the aim of the optimization process.

The convergence criterion for the objective function $\Phi$ is defined by the minimum change of the parameters as a percentage of their initial value. The progress of the summarized objective function and its main components (without weighting factors) is shown in Figure 10. It should be noted, that the optimization process is based on a Simplex algorithm (Nelder and Mead (1965)).

## *Optimization results*

After convergence of the process, the updated finite element model is postprocessed in two parallel steps: automated generation of manufacturing documents, which includes a detailed ply book of the droop nose skin, and geometric optimization of the inner kinematic mechanism. An example of the FE model for a morphed skin and a CAD assembly of the related demonstrator are shown in Figure 9.

The design of the droop nose kinematic mechanism is implemented according to the method that is described by Kintscher and Heinze (2010). Thereby, the trajectories of the force application points are applied to define a geometrical solution for the position of kinematic joints as well as for the position and traverse angle of a rotary actuator. The levers of the kinematic system are assumed to be rigid. The geometrical results of the skin optimization are presented in Figure 10. It can be seen that the deviation from the target shape is relatively small (max. deviation approx. 3 mm) for both numerical results with and without applied aerodynamic loads. The subsequent optimization of

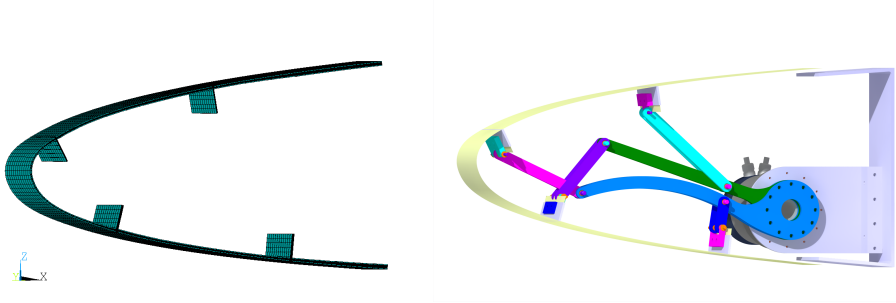

**Figure 9.** Finite element model of the skin (left) and the CAD model of the actuation system (right).

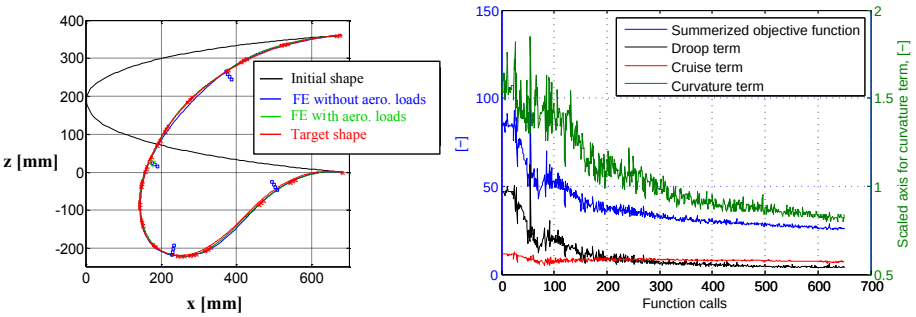


**Figure 10.** Results and convergence behaviour of the optimization.

the inward kinematic system (last step in Figure 7) increases the maximum deviation to approx 7 mm due to geometry restrictions of the hinge-struts kinematic.

## Results

The main aim of structural testing of the morphing leading edge is a demonstration of structural feasibility of an adaptive high-lift device for an actively blown Coandă-flap wing. Therefore, the numerical results of the above mentioned optimization process were implemented in a functional full-scale demonstrator of the leading edge. The extruded 2D airfoil (0.1 m span section) is taken from the inner part of the outer wing near the kink (located at 40% span 6.50 m from the centerline with 3.36 m chord). The kinematic station is equipped with a torque actuator drive for deployment of the morphing leading edge device. The full-scale 2D demonstrator is presented in Figure 11.

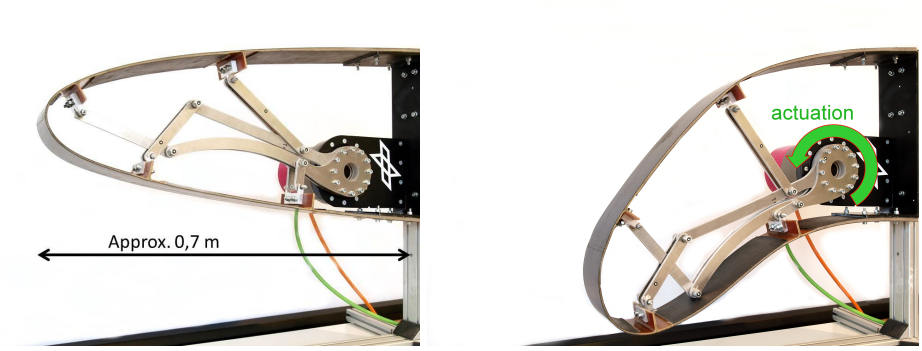


**Figure 11.** Full-scale droop nose demonstrator.

## *Experimental setup*

There are two main goals of the structural test: one is the measurement of the structural deformation into the desired position without aerodynamic loads for further aerodynamically assessment of a real morphed structure. The other one is the validation of the FE model and optimization process chain for large displacements with measured strain of the hybrid composite skin.

The optical measurement of the structure in undeformed and deformed conditions is performed with the measurement system ATOS Triple Scan of the GOM Company. The result is a surface mesh of the structure in both conditions.

Additionally, 18 strain gauges are applied to the structure along the airfoil perimeter inside of the hybrid skin to achieve local strain information. The sensors are placed on the outer ply of the GFRP middle section, cp. Figure 3, to measure the maximum bending strain in the strength-relevant component of the hybrid skin structure.

## *Optical measurements*

The results of the optical measurement (presented in Figures 12 and 13) are compared with FE simulation results to find and evaluate the deviations of the shapes. To represent an evaluation criteria, the maximum values of shape differences can be roughly summarized to

$$\Delta_{total} = \Delta_{manufacturing} + \Delta_{simulation} \tag{4}$$

The output of the optical measurement of the leading edge demonstrator in undeformed condition is presented in Figure 12. The CAD export of the initial wing shape is applied as a reference to identify the geometrical deviation to the surface of

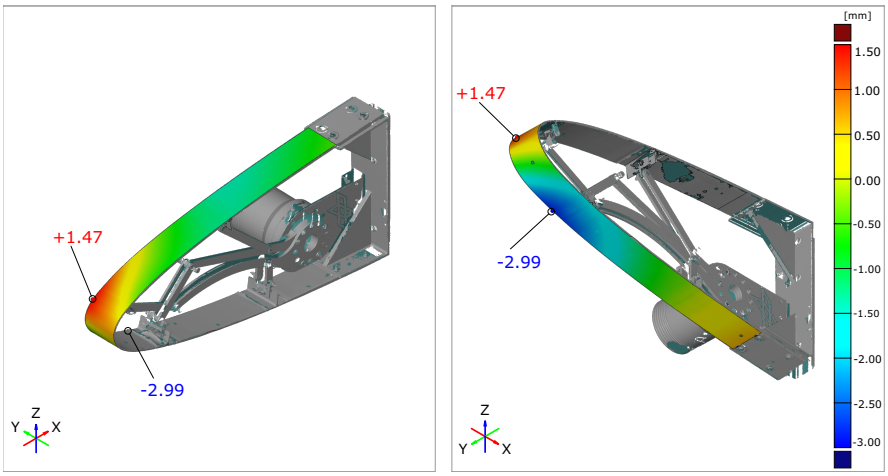


**Figure 12.** Measured deviation of the demonstrator skin from the ideal FE model without morphing deflection.

the manufactured skin. To align the measurement and numerical meshes, a local best-fit algorithm (implemented in the GOM software) is used.

The positions of maximum difference between the numerical and experimental results are highlighted according to the legend. The deviations are resulting from assembly and manufacturing processes of the demonstrator and can be rated as moderate in proportion to the component size:

$$-2,99 \text{ mm} \leq \Delta_{manufacturing} \leq 1,47 \text{ mm} \tag{5}$$

Nevertheless, they have to be taken into account for an assessment of shapes and structural loads of the morphed leading edge structure. Based on the characteristic distribution of the deviation areas, a high sensitivity of $\Delta_{manufacturing}$ to the mounting precision of the skin on the spar is identified. However, this issue should decrease with higher span length of the leading edge due to a higher shear stiffness of the component.

The experimental results of the deformed leading edge are presented in Figure 13. In that case the reference is derived from the result of a non-linear finite element simulation of the demonstrator with implemented kinematics. In this case as well, the CAD and finite element meshes are aligned by the local best-fit algorithm of the GOM Inspect software. The maxima of the geometrical deviation are relatively large with:

$$-5,24 \text{ mm} \leq \Delta_{total} \leq 6,64 \text{ mm} \tag{6}$$

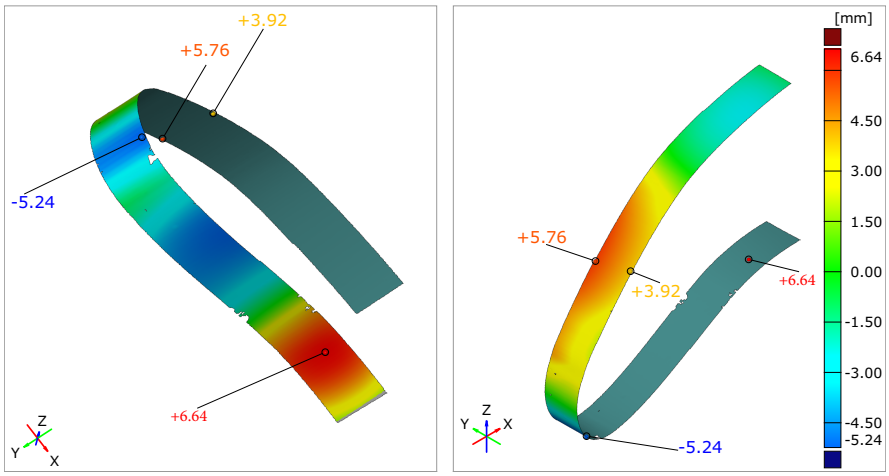


**Figure 13.** Measured deviation of the demonstrator skin from the simulation prediction at full morphing deflection.

Compared to the distribution of deviations in undeformed condition, the maxima are now determined by structural behaviour of the component: the areas with highest level of $\Delta_{total}$ are concentrated between the force application stringers, where the structure is forced to position by the kinematic system. The influence of $\Delta_{manufacturing}$ can be seen in the asymmetry of the distribution on the top region of the morphed wing, with a gradient of $1.84\ \mathrm{mm}$ per $0.1\ \mathrm{m}$ span. This corresponds to the influence of $\Delta_{manufacturing}$, that was identified before.

With a high degree of probability, the reasons for a relative high $\Delta_{simulation}$ can be found within the FE-model simplifications. Especially the modeling of force introducing stringers with shell elements (implemented to reduce computational costs of the optimization procedure) can be identified as a possible source of imprecision due to a highly 3D shape of these components.

## *Strain measurements*

The strain measurement results are compared with FE-results for selected locations of the skin in order to validate the optimization process chain. The comparison presented in Figure 14 is based on strain value distributions in peripheral direction, beginning at the bottom spar attachment of the leading edge skin. The strain gauges are located in the middle of the skin in span-wise direction on the inner GFRP layer of the hybrid skin - the expected location of the highest strain level. The measured peak values of $\epsilon_{experimental} = [-1.5\%, +1.47\%]$ are below the strain at rupture of the

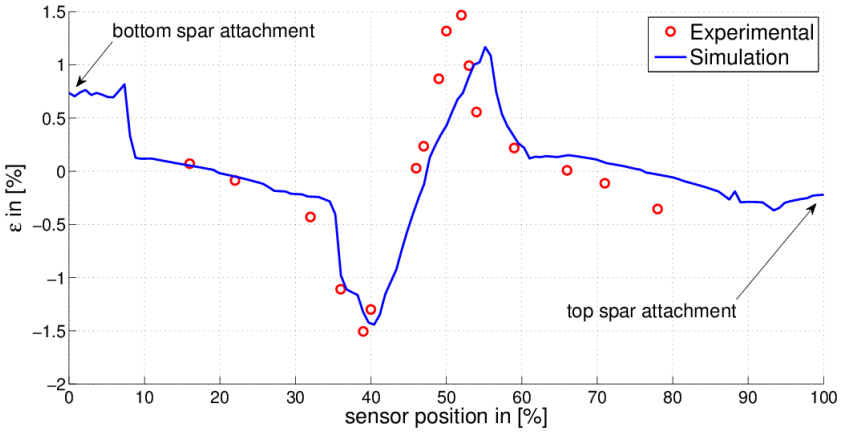


**Figure 14.** Comparison of measured and simulated strains in normalized peripheral direction of the skin.

GFRP segments, but are noticeable higher than the simulation prediction ($\epsilon_{simulation} \in [-1.44\%, +1.17\%]$). The progressions of strain curves are also displaced relatively to each other, especially on the top panel of the airfoil. Some possible reasons for such behavior are already mentioned in the previous section: both existing assembly issues and model simplifications appeared to have significant influence on the simulation quality within the optimization process.

## Conclusions and Outlook

In this study, a full-scale adaptive leading edge section is designed as a result of an automated optimization process with the use of hybrid GFRP-Elastomer structures. Based on structural optimization considering actuation mechanisms and aerodynamic loads for the most relevant points of the flight envelope, a drive test prototype is designed and manufactured. Manufacturable skin segments are defined a priori and placed along the leading edge perimeter by optimization. Beside a centred GFRP stacking, the presented skin structure features additional hybrid layers which drastically increase the skin stiffness in span-wise direction. This, however, will become most relevant in the next steps of creating a fully 3D leading edge segment (approx. 2 m span). Successful actuation is demonstrated by a drive test with extremely large deformation amount of morphing. The shapes of the demonstrator in undeformed and full-morphed conditions are compared to numerical results and the sensitivity towards assembly deficiencies and model simplifications are investigated. Strain measurements are performed and compared to simulations. The sensitivity of the presented design

process towards model quality is shown and the necessity of more precise modelling of force introduction stringers is determined. In particular, a one-node-line connection between the stringer and the skin shells was identified to have limited capability to map the stiffness behaviour of the component. A 3D-modelling of the skin and stringers or an implemented reduced-order model of the interface could be a solution of this issue.

## Acknowledgements

Funding for this work is provided by the German Research Foundation (DFG) through the Collaborative Research Center (SFB) 880 “Fundamentals of High Lift for Future Civil Aircraft”. The authors would like to thank everyone involved in the presented research.

## References

ACARE 2050 (Advisory Council for Aviation Research and Innovation in Europe) (2011) *Flightpath 2050 Europe’s Vision for Aviation*, Publications Office of the European Union, Luxembourg, p. 15.

Ajaj RM, Friswell MI, Bourchak M, Harasani W, Span morphing using the GNATSpar wing, *Aerospace Science and Technology* vol. 53, pp. 38–46

Barbarino S et al. (2011) A review of morphing aircraft. *Journal of Intelligent Material Systems and Structures* 22(9):823–877.

Burnazzi M and Radespiel R (2014) Assessment of leading-edge devices for stall delay on an airfoil with active circulation control, *CEAS Aeronautical Journal*, Volume 5, Issue 4, pp. 359-385.

De Gaspari A and Ricci S (2011) A Two-Level Approach for the Optimal Design of Morphing Wings Based On Compliant Structures, *Journal of Intelligent Material Systems and Structures*, 22(10):1091-1111.

Federal Aviation Administration (2015) United States Aviation Greenhouse Gas Emissions Reduction Plan. Availible at: https://www.faa.gov/nextgen/update/progress_and_plans/environment/ (accessed 01 November 2016)

Falcão L, Gomes AA and Suleman A (2011) Aero-structural Design Optimization of a Morphing Wingtip, *Journal of Intelligent Material Systems and Structures*, 22(10):1113-1124.

Gamboa PV and Santos PD (2016) Telescopic Wing-Box for a Morphing Wing, *24th AIAA/AHS Adaptive Structures Conference, AIAA SciTech Forum*, San Diego, USA

Heinze, W and Radespiel R (2014) SFB 880 - fundamentals of high-lift for future commercial aircraft, *CEAS Aeronautical Journal*, vol. 5, no. 3, pp. 239-251 DOI 10.1007/s13272-014-0103-6

Lu, KJ and Kota, S (2005), An effective method of synthesizing compliant adaptive structures using load path representation *Journal of Intelligent Material Systems and Structures*, vol 16, no. 4, pp. 307-317. DOI: 10.1177/1045389X05050104

Kintscher M, Heintze O and Monner HP (2010) Structural Design of a Smart Leading Edge Device for Seamless and Gapless High Lift Systems, *1st EASN Association Workshop on Aerostructures*,Paris, France.

Kintscher M et al. (2015) Assessment of the SARISTU Enhanced Adaptive Droop Nose, *Smart Intelligent Aircraft Structures (SARISTU)*, Springer International Publishing pp. 113-140.

Kreth S, König R and Wild J (2007) Aircraft noise determination of novel wing configurations, *Inter-Noise2007*, Istanbul, Turkey.

Nelder JA and Mead R (1965) A Simplex Method for Function Minimization *The Computer Journal* 7 (4): 308-313

Radestock M et al. (2015) Experimental Investigation of a Compliant Mechanism for an UAV Leading Edge, *SMART 2015. 7th Eccomas thematic conference on Smart Structures and Materials*. Ponta Delgada, Acores, Portugal.

Schmitz A and Horst P (2014) A new curvature morphing skin: manufacturing, experimental and numerical investigations, *16th European Conference on composite materials*, Seville, Spain.

Schmitz A and Horst P (2014) A finite element unit-cell method for homogenised mechanical properties of heterogeneous plates, *Composites: Part A*, 61:23-32.

Schmitz A and Horst P (2015) Development and investigation of a hybrid curvature-morphing skin structure, *20th International Conference on composite materials*, Copenhagen, Denmark.

Schmitz A and Horst P (2015) Buckling of multiple discrete composite bundles in the elastomeric foundation of a curvature-morphing skin, *Composite Structures*, 134:1014-1023.

Sun J, Guan Q, Liu Y and Leng J (2016) Morphing aircraft based on smart materials and structures: A state-of-the-art review, *Journal of Intelligent Material Systems and Structures*, doi:10.1177/1045389X16629569.

Takahashi H, Yokozeki T and Hirano Y (2016) Development of variable camber wing with morphing leading and trailing sections using corrugated structures, *Journal of Intelligent Material Systems and Structures*, doi:10.1177/1045389X16642298.

Vasista S et al. (2016) Compliant structures-based wing and wingtip morphing devices, *Aircraft Engineering and Aerospace Technology: An International Journal*, 88(2):311-330.

Weisshaar T (2013) Morphing Aircraft Systems: Historical Perspectives and Future Challenges, *Journal of Aircraft*, 50(2): 337-353.